

Simulations of Strong Ground Motion and 3D Amplification Effect in the Taipei Basin by Using a Composite Grid Finite-Difference Method

by Shiann-Jong Lee, How-Wei Chen, and Bor-Shouh Huang

Abstract We perform full elastic wave-field simulations within the Taipei basin by using a three-dimensional (3D) discontinuous finite-difference method. The 3D Taipei basin model is determined from a seismic reflection study. Two major subsurfaces, the Songshan formation (surface soil layer) and the basin basement, are constituted in the model. A parallel-based composite grid technique, a containing scalene grid and a discontinuous grid, is developed in this study to deal with the possible numerical problem of thin depth and low velocity of the Songshan formation. Taking advantage of the composite grid, the resolution of the subsurface structure can be reached to 20 m, and a higher frequency (up to 3 Hz) of the synthetic waveform can be achieved. In our strong ground motion simulations, we assume a constant velocity in each subsurface. Three different types of models are considered in the study: the Songshan formation with a basement structure model, a basin basement model, and a layered half-space model. Results indicate that only the model with both the Songshan formation and the basement structure can produce the apparent basin amplification effects. First, the surface wave generated after the primary S wave is trapped at the shallow part of the basin. Then, when the wave propagates through the deepest part of the basin, most of the energy is reflected from the boundary and focused back into the basin. In addition, part of the seismic wavefront turns and follows the shallow basin edge resulting in further amplification. Our study indicates that the complex Taipei basin geometry and fairly low velocity of the Songshan formation dominate the amplification and wave propagation behavior that result in extraordinary strong shaking patterns in the Taipei metropolitan region.

Introduction

The city of Taipei is built upon a sedimentary basin in northern Taiwan that is made up of Quaternary alluvium and lake deposits. Seismic disasters in the Taipei basin over the last 20 yr, particularly during the 1999 Chi-Chi earthquake (M_L 7.3) and the 31 March 2002 east coast earthquake (M_L 6.8) caused significant building damage and collapse events with considerable casualties (Wen *et al.*, 1995; Wen and Peng, 1998; Chen, 2003). Although these earthquakes are located more than 100 km from the basin, the shaking intensity within the basin is even larger than some areas near the epicenter. The unconsolidated sediments in the Taipei basin are made up of alluvial deposits from the TanShui River, and the youngest deposit, the Songshan formation, is formed by a layer of relatively thin depth (about 50 m) with a fairly low S -wave velocity. Previous studies concerning basins indicate that low velocity materials and basin geometry have a strong influence on the behavior of seismic-wave propagation (Yomogida and Etgen, 1993; Alex and Olsen, 1998; Davis *et al.*, 2000) and strengthen/lengthen shaking activity (Olsen *et al.*, 1995, 1996; Olsen, 2000; Graves 1998;

Komatitsch *et al.*, 2004). Taipei basin's soft surface layers, in particular, make the heavily populated city particularly vulnerable to severe earthquake damage.

The Taipei basin amplification effect can be controlled further by several factors that vary with the varying basin structure. Numerical simulations have been successfully used to study the complex nature of strong-motion wave propagation in basins (Olsen *et al.*, 1995, 1996; Olsen, 2000; Graves, 1998). Because of a lack of empirical strong ground motion observations, theoretical simulations constitute our best hope of addressing this issue. From the results of combining seismic reflective profiles and borehole data (Wang *et al.*, 2004), we have established a high-resolution basin geometry model with a resolution as fine as 20 m to estimate the 3D seismic response of the Taipei basin. We put emphasis on the response to the surface soil and basin geometry by considering a simple point source. Results can be generalized to extended sources. To distinguish the case of the amplification effects, three models with different hypotheses are analyzed. Ground-motion behavior in the Taipei ba-

sin derived from a regional scenario earthquake is then presented. We analyze the wave propagation snapshot, synthetic waveform, amplification characteristics of peak ground velocity (PGV), and cumulative kinetic energy. Finally, we point out the possible amplification factors in the Taipei basin based upon our numerical simulation results.

Basin Model and Numerical Method

Taipei Basin Model

The Central Geological Survey of Taiwan has conducted a wide range of investigations of the Taipei basin by drilling over 30 wells (100–700-m deep) during the past 10 yr. Recently, Wang *et al.* (2004) scanned the basin area (20 × 20 km) using over 300 shallow reflection seismic lines to combine the seismic data and the borehole drilling results to better describe the Tertiary basement, the Quaternary layers above the basement, and their *P*- and *S*-wave velocities. The results of this digital basin model are shown in Figure 1. Several characteristics can be noted: (1) the Taipei basin is a shallow dish-shaped basin with a gentle dipping boundary and the average dipping angle is not more than 45°; (2) the deepest part of the basement is probably near the outlet of the TanShui River in the northwest area of the basin; (3) the KanChiao fault forms a boundary bisecting the basin into a deep northwest and a shallow southeast division; (4) the surface layer, the Songshan formation, is relatively shallow with flat deposits on the top; and (5) the whole

basin is inclined toward the northwest–western boundary and is marked by the SanChiao fault. The *P*- and *S*-wave velocities inside the basin (including the Songshan formation) are, respectively, about 450–2200 and 170–880 m/sec; velocities of the basin basement (Tertiary basement), which is beneath and surrounding the basin, are 3000 and 1500 m/sec, respectively. For the purpose of numerical simulations, we use two major discontinuities separating layers of homogeneous velocities: one being the Songshan formation and the other being the basin basement. The deepest part of the Songshan formation is only about 120 m. However, the basement depth extends to more than 700 m (Fig. 1a and b).

Parallel-Based Composite Grid

A modified elastic finite-difference code (Chang and McMechan, 1987, 1994) for 3D wave-field simulation is used in predicting ground motion. The in-house developed numerical program is further modified to incorporate more realistic double-couple source characterization and with more effective absorbing condition (Lee *et al.*, 2007). A numerical difficulty will arise when analyzing the wave propagation behavior in the Taipei basin because of the thin depth and fairly low *S*-wave velocity of the Songshan formation. To deal with this problem, we develop a parallel computing based composite grid technique. The grid system in this scheme contains two domains, one is a scalene grid and the other is a discontinuous grid (Fig. 2). Considering the

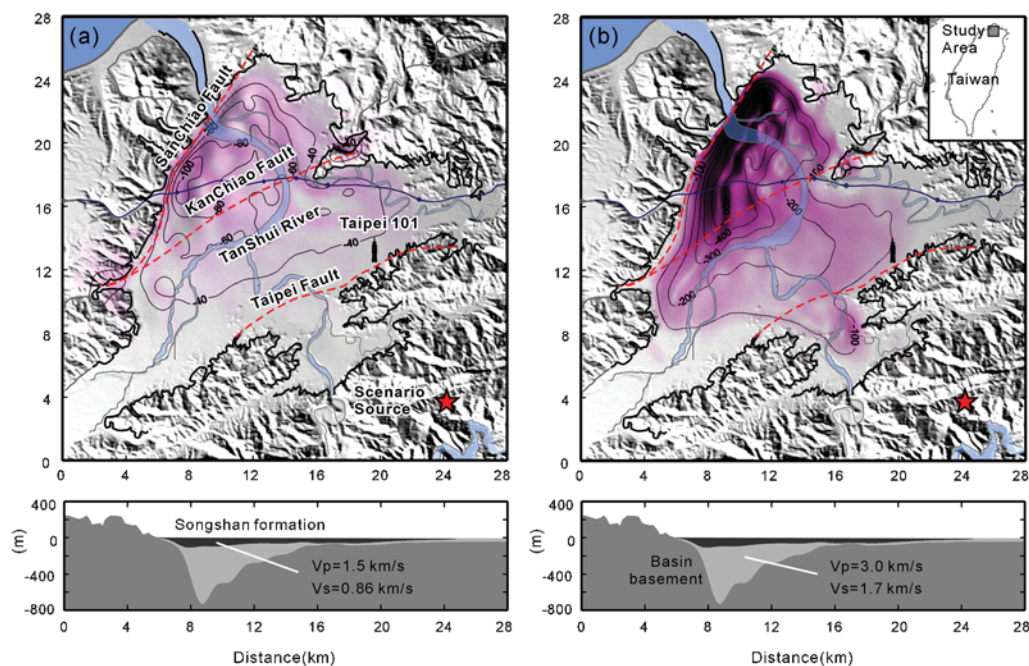


Figure 1. The main subsurface of the Taipei basin. (a) Depth distribution of the Songshan formation. The contours show the isodepth and the red dotted lines indicate the major fault systems in the basin. (b) Tertiary basement depth distribution. The scenario source location is shown as a star in the figure. The National Freeway 1 is shown by the blue line. Taipei 101, currently the tallest building in the world, is also marked in the figure. Lower panels are the side view from southerly direction of the Songshan formation and basement. The *P*- and *S*-wave velocities used in the simulations are indicated in the figure.

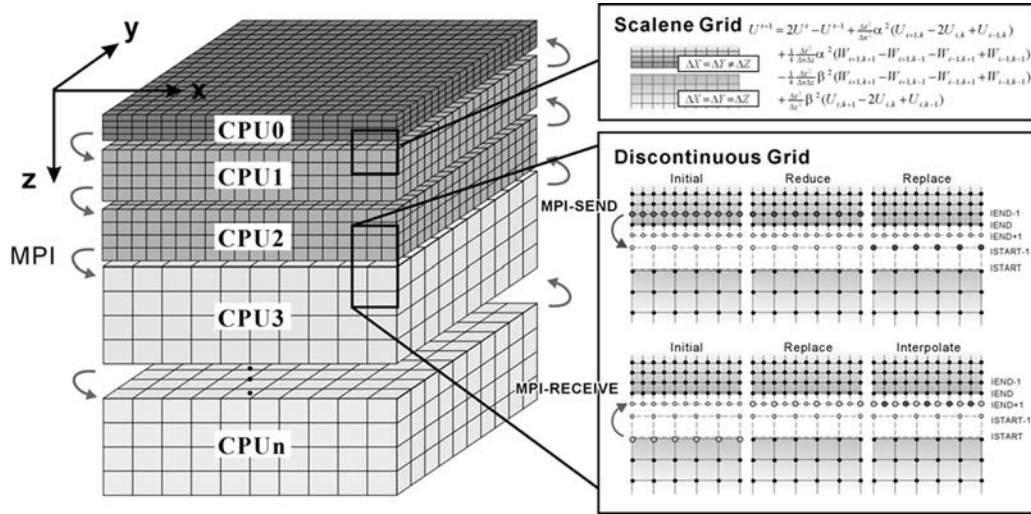


Figure 2. Composite grid scheme. The domain decomposition is based on an N -node parallel environment. Three domains with different grid systems are set in the computing model. For depth less than 240 m, the scalene grid ($dz = 10$ m) is used to constrain the Songshan formation. At 840 m, the discontinuous grid is applied to deal with the limitation of memory capacity. The data exchange required for different domains is performed by the MPI.

U -component 3D wave equation with second-order finite-difference approximation,

$$\begin{aligned}
 U_{x,y,z}^{t+1} = & 2U_{x,y,z}^t - U_{x,y,z}^{t-1} \\
 & + \frac{\Delta t^2}{\Delta x^2} V_p^2 (U_{x+1,y,z}^t - 2U_{x,y,z}^t + U_{x-1,y,z}^t) \\
 & + \frac{\Delta t^2}{4\Delta x \Delta y} (V_p^2 - V_s^2) (V_{x+1,y+1,z}^t - V_{x+1,y-1,z}^t \\
 & - V_{x-1,y+1,z}^t + V_{x-1,y-1,z}^t) \\
 & + \frac{\Delta t^2}{4\Delta x \Delta z} (V_p^2 - V_s^2) (W_{x+1,y,z+1}^t - W_{x+1,y,z-1}^t \\
 & - W_{x-1,y,z+1}^t + W_{x-1,y,z-1}^t) \\
 & + \frac{\Delta t^2}{\Delta y^2} V_s^2 (U_{x,y+1,z}^t - 2U_{x,y,z}^t + U_{x,y-1,z}^t) \\
 & + \frac{\Delta t^2}{\Delta z^2} V_s^2 (U_{x,y,z+1}^t - 2U_{x,y,z}^t + U_{x,y,z-1}^t). \quad (1)
 \end{aligned}$$

In the normal grid domain, the grid sizes at three components are the same; this means $\Delta x = \Delta y = \Delta z$ in equation (1). However, in the scalene grid domain, the grid size at the vertical (z) component is different from x and y , that is, $\Delta x = \Delta y \neq \Delta z$. By this approach, we can have a smaller grid size at the shallow part along the vertical direction and, thus, improve the model resolution and simulation accuracy in the basin.

We further combine discontinuous grids with different grid size domains in different computing nodes based upon the parallel computing technique (Fig. 2). In the fine grid domain, the wave fields at the second to the last vertical elements (IEND-1) are reduced to contrast with the elements in the rough grid domain. The reduced grid values are then

passed to the padded elements (ISTART-1) at the first node of rough grid domain. In the opposite direction, the first vertical elements (ISTART) in the rough domain are sent to the padded array (IEND+1) at the last node of fine grid domain and then interpolated by using the interpolation method of Aoi and Fujiwara (1999). Using this approach, the grid size is changed in all three components with respect to different grid domains. All the reduced and interpolated values are communicated by using a message passing interface (MPI, Gropp *et al.*, 1996). These values sent/received between scalene and discontinuous grid domains then follow the finite-difference formula to update the current wave fields for the transition elements. Finally, the reduction, interpolation, and message passing communication are iterated during the simulation process in the whole model.

To examine the stability of the parallel-based composite grid scheme, we conduct a bench-mark test by considering half-space and layered velocity structures with both ordinary and composite grid models (Fig. 3). A double-couple point source with strike-slip mechanism is set beneath a discontinuous grid domain, that is, in the normal grid domain, to help in examining the stability when the waves propagate through the interfaces of two different grid domains. We give a linear receiver array along the direction of N45°E from the epicenter with an interval of 1.414 km. Figure 3a compares the vertical velocity wave-field snapshots at 1.25 sec and the synthetic waveforms between two different grid systems in the half-space model. The two snapshots are almost the same, which show clear P - and S -wave and surface reflections. By applying the scalene grid at the shallow part of the model, the receiver locations can move closer to the free surface because of a smaller dz in the scalene grid compared to the ordinary grid. As can be noticed in the synthetic waveforms, there are some discrepancies between two sets of

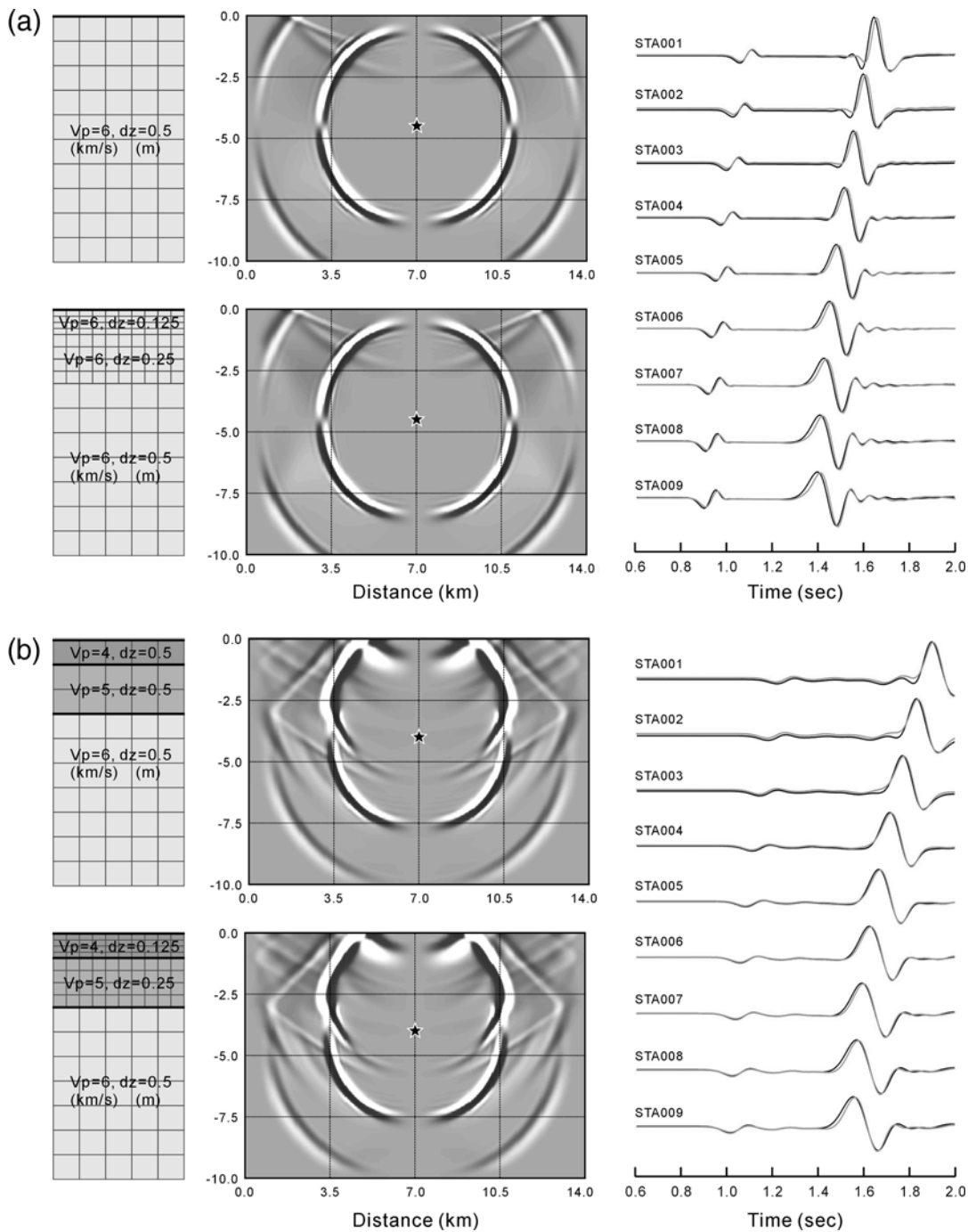


Figure 3. Bench-mark tests of parallel-based composite grid scheme: (a) half-space homogeneous model ($V_p = 6$ km/sec); (b) layered velocity model ($V_p = 4, 5,$ and 6 km/sec, respectively). The size of the model is $10 \times 10 \times 10$ km³. S -wave velocity is computed from the P -wave velocity by assuming a Poisson solid. Two different grid models are considered, one is a composite grid and the other is an ordinary grid. A double-couple strike-slip source is set in the normal grid domain. Left panels show the grid settings in the models. Middle panels are the velocity wave-field snapshots across the diagonal profile at 1.25 sec. The vertical component synthetic waveforms on a receiver array (with an interval of 1.414 km) along N45°E from the epicenter are shown in the right panels. Black and gray lines are the synthetic waveforms derived from composite and ordinary grid models, respectively.

waveforms that result from higher accuracy of receiver positions in the scalene grid. We further consider a layered velocity structure to test the stability between two different grid models (Fig. 3b). The wave field of the layered model is complex compared to the half-space model, but again, the

snapshots between two grid systems are exactly the same. We also see the discrepancy between two sets of the synthetics, which is due to different grid accuracy at the free surface. In general, the bench-mark results of the composite grid show good stability in both wave-field snapshots and

synthetic waveforms. By the parallel-based composite grid scheme, we save 75% of the used grid as compared to the ordinary grid model. This enables us to deal with the wave propagation problem considering the shallow and low velocity sedimentary layer in the basin with a higher resolution.

Simulation Settings

We examine the seismic response of the Songshan formation and basin geometry. The velocity outside the basin is simplified by an assumption of a homogeneous half-space. The dimension of the simulated Taipei basin model is 27.8 × 27.8 km at the surface and 3.72 km in depth. To achieve the half-space simulation outside the basin in this thin model, we adopt a composite boundary comprising the A_2 boundary condition (Clayton and Engquist, 1977) and the nonreflection boundary condition (Cerjan et al., 1985) at the model boundary. A double-couple point source is placed at the southeast (24.2 km, 3.8 km) with a depth of 1.0 km. The source focal mechanism is defined as strike 0°, dip 90°, and rake 0°. For this strike-slip point source, the radiation pattern is well known in the study area that would have the largest amplitudes along the northwest direction for P and SV phases. We attempt to examine the comprehensive basin effects according to the body and surface waves excited from this well-controlled earthquake. A Gaussian source time function with a duration of 0.3 sec is set to a response frequency to about 3 Hz. High-velocity ratios between sub-surfaces are given in the model to emphasize the influence of Songshan formation and basement geometry. The average P -wave velocity in the Songshan formation is 1.5 km/sec, between the Songshan formation and the basement is 3.0 km/sec, and the bedrock outside the basin is 4.5 km/sec. We simplified the S -wave velocity that is computed from the P -wave velocity by assuming a Poisson solid. Because of the lack of anelastic attenuation and density tomography information, we assume constant Q and density within and outside the basin. Attention is paid to the influence of lateral wave propagation on the current basin geometry and anelasticity is temporarily ignored in the study.

Under the framework of the composite grid, the whole Taipei basin model is divided into three domains, each with different grid sizes. To preserve the highest resolution of the

Songshan formation boundary, especially in depth, the scalene grid ($20 \times 20 \times 10 \text{ m}^3$) is applied to cover the overall formation in the basin. A normal grid is set between the Songshan formation and basin basement. We applied a discontinuous finite-difference grid beneath the basement to save computing memory and prepare for the future simulation that will incorporate the Moho and other subsurface. In this case, the grid size in the second (normal) grid domain is 20 m and then doubled to 40 m for the half-space below 840 m, which is under the deepest part of the basin. The total used grid in the model is about 188 million, requires 9.5 GB of distributed memory. On the IBM eServer (BladeCenter, 10 nodes, 20 processors), the average computing time for a 50 sec simulation is about 36 hr. The detailed P and S -wave velocity properties and simulation parameters are listed in Tables 1 and 2, respectively.

Simulation Result

Wave-Field Snapshot

We analyze the wave propagation behavior by computing the ground velocity snapshots with durations of 50 sec. Figure 4 shows the snapshots of the vertical component velocity wave field at every 5 sec. When the wave enters the Taipei basin, the travel time of the wavefronts is delayed and distorted. Because of the low velocity in the basin, especially within the Songshan formation, the wavefronts slow down compared to those outside the basin. At 10 sec, surface waves (Rayleigh waves) that propagate after the S wave can be observed. Surface waves are generated by the reflections and mode conversions between the Songshan formation and the free surface. At the same time, the energy is trapped and reflected within the shallow part of the basin. However, P -wave energy is relatively weak at this moment and passes through the basin quickly as compared to the later S -wave and surface wave phases. When the seismic wave reaches the northwest boundary, at about 15 sec, most of the energy cannot pass through the sharp boundary, and then must rebound back into the basin. The energy interference seems to set up resonance temporarily at the northwest edge, which is particularly clear during 20–25 sec. After 25 sec, energy begins to radiate toward the south and east directions. The southern spreading energy propagates back into the basin

Table 1
 P - and S -Wave Velocities Used in the Simulations

	Depth (m)	P Wave (m/sec)	S Wave (m/sec)
Songshan formation	0–120	1500 (450–1500)	866 (260–866)
Songshan formation–Tertiary basement	120–700	3000 (3000)	1732 (1732)
Tertiary basement	> 700	4500 (4500)	2598 (2598)

The values in brackets are the range of velocities within the laterally heterogeneous velocity model as considered in the section Simulations of the Real Data.

Table 2
Simulation Parameters

Parameter	Value
Spatial discretization (km)	0.02
Temporal discretization (sec)	0.002
Lowest <i>S</i> -wave velocity (km/sec)	0.86
Grid size (grid points)	$\sim 1400 \times 1400 \times 96 = 188.16 \times 10^6$
Number of timesteps	25,000
Simulation time (sec)	50
Memory usage (GB)	9.5
Computation time (hr)	~ 36

The computation time is determined by using the IBM eServer (10 nodes, 20 processors) at IESAS.

while the eastern spreading energy goes through the surrounding mountain. During 35–40 sec, parts of the eastern radiated energy go into the basin again, and then the propagated direction turns along with the eastern basin edge. This behavior results in the local amplification and further prolongs the ground shaking time. It is noticeable that this phenomenon is adjacent to one of the populous high-rise areas in Taipei city near Taipei 101 (currently the tallest building in the world). The overall strong shaking in the basin continues for about 50 sec.

In this simulation, the main wave propagation characteristics are (1) strong surface waves are generated after the *S* wave by the reflected and trapped energy between the soft sedimentary layer; (2) most of the seismic waves rebound from the basin boundary and set up reverberations at the deepest part of the basin; and (3) as reverberations die out, waves are radiated eastward and southward. During this period, the energy on the deepest part of the basin continues oscillating with a resonance period of about 2 sec.

Synthetic Waveform

The 3D finite-difference synthetic seismograms for sites corresponding to the strong-motion network in the Taipei metropolitan region are shown in Figure 5. Solid squares are Central Weather Bureau (CWB) strong-motion stations; light gray squares represent a pseudoarray across the basin. The location of this pseudoarray is chosen to go across the main basin structure. From west to east, this array crosses the SanChiao fault, the deepest part of the basin, the KanChiao fault, and the eastern edge of the basin. The synthetic velocity waveforms are band-pass filtered from 0.01 to 3 Hz and normalized with the largest amplitude of the synthetics. These waveforms show anomalous amplifications in the basin. Stations near the epicenter (e.g., TAP033, TAP101, TAP071, and TAP097) show large amplitudes that are mainly influenced by the source radiation. However, the stations within the basin that have a larger epicenter distance also show strong shaking, for example, at TAP004, TAP006, TAP051, and TAP099. These stations show the amplification effects associated with the soft sediment and the basin geometry. The influence of the basin is not shown only in ampli-

tude but also in the ground-motion duration. It is obvious that the synthetic waveforms in the basin have a relatively longer duration as compared to the stations outside the basin, especially for the records on station at TAP004 and TAP016 near the deepest part of the basin. The strong shaking times of these synthetics are prolonged for more than 30 sec. This phenomenon might be related to the trapped energy and resonance at the western basin. Some stations, such as TAP004, TAP096, TAP006, and TAP093, have a strong secondary phase behind the surface wave. This phase is likely to come from reflections from the basin boundary.

We have analyzed the maximum particle velocity on the surface to obtain the information on PGV distribution. Figure 6a, b, and c shows the east, north, and vertical component of PGV distribution within the basin, respectively. For a strike-slip point source with a strike of 0° , the *P* wave would show the largest amplitude at the vertical component, and the *SH* wave would have the largest amplification at the east and north components. The PGV distributions in each component follow the theoretical radiation pattern reasonably well, but they do not show an obvious basin response. Although the velocity waveforms in the basin have apparent amplification in our analysis, the near-field PGV distribution is mostly dominated by the source radiation pattern.

Cumulative Kinetic Energy

The PGV does not reflect the basin amplification effect when the epicentral distance is comparable to the source dimension. Here, we consider another parameter named E_k , or cumulative kinetic energy. This parameter is obtained by summing the square of the velocity amplitude of all three components in the seismogram in time, multiplying the density ρ , then dividing by 2. The cumulative kinetic energy per unit volume of the *k*th-component trace is given as

$$E_k = \frac{1}{2} \rho(x, y) \int \dot{u}_k^2(x, y, t) dt, \quad (2)$$

where E_k reflects the amplitude and duration time of the total motion that may be more closely related to the shaking damage potential (Olsen *et al.*, 1995, 1996). The distribution of

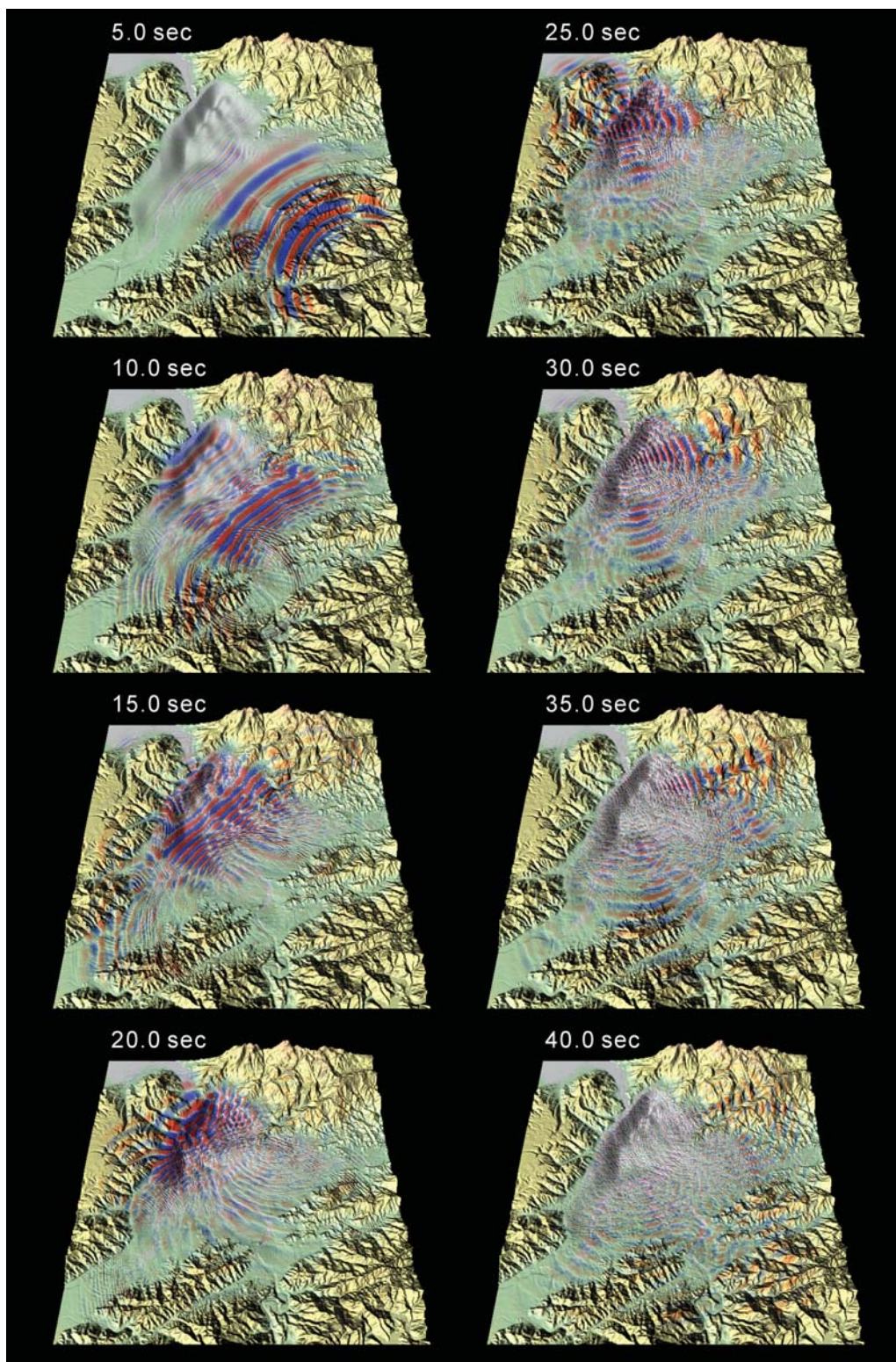


Figure 4. Snapshots of the vertical component ground motion at $T = 5, 10, 15, 20, 25, 30, 35,$ and 40 sec, calculated by the composite finite-difference method. Red (blue) shading depicts positive (negative) particle velocity. The amplitude is scaled for a constant for all snapshots. Surface topography and perspective basin basement structure are shown for the comparison. The result produces clear spatial-temporal dependence of the basin effect pattern.

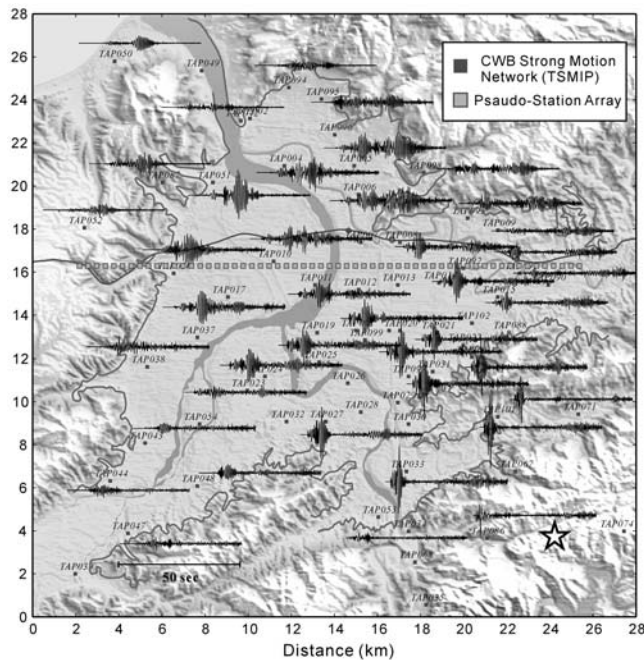


Figure 5. Strong-motion network and synthetic waveforms in the Taipei basin. Solid squares are TSMIP stations; light gray squares represent a pseudoarray across the basin. The star is the epicenter of a simulation earthquake. A subset of the synthetic waveforms is shown in the figure. The timescale of the synthetic waveform is indicated by the scale bar at the bottom. It is obvious that the velocity waveforms in the basin have larger amplitudes and longer duration times as compared to that of stations outside the basin.

E_k shown in Figure 6d is unusually large in the basin, especially at the northwest part. The large E_k originates from the source and moves across the basin. Because most of the energy is trapped in the deepest part, the largest E_k happens to be near the northwest boundary of the basin. The eastern basin also has large E_k that is due to the energy that turns and propagates along the basin boundary as described in the snapshot analysis. This result shows that the cumulative kinetic energy E_k more accurately reflects the apparent basin effect than a PGV.

We have analyzed a suite of seismograms and the relative velocity structure along the pseudoarray (the light gray squares in Fig. 5) to show the overall basin effects where an obvious relation between basin structure and the amplitude and duration of the synthetic waveforms is found (Fig. 7). The strong shaking duration time increases with the depth of the basin from east to west. Three particular phases can be found from the travel-time diagram; they are the P wave (P), the S wave (S), and the Rayleigh wave (R). All of these phases are influenced by the basin effect, which demonstrates larger amplitudes, later complex reflections, and longer duration times according to the basin depth. There is another phase (X) in which we can trace its travel time after the surface waves. This phase does not follow the expected travel-time curve. The cause of this phase is the result

from the reradiation of energy from the wave trapped in the deepest part of the basin where the travel time of this phase originated. Figure 8 shows the PGV and E_k result along the pseudoarray. Because PGV is easily influenced by source radiation, it does not show clear relationships with the basin. To investigate the basin amplification effect, we should examine the cumulative kinetic energy. The result clearly shows the average E_k value within the basin is larger than that outside the basin, especially at the western boundary. There are some exceptionally large E_k at specific locales. These locations are most likely related to the path effect that bends, and thus focuses, the rays. The detailed amplification behavior in the basin is complex and is clearly contributed by several model factors.

Discussion

Validation of Basin Amplification Effects and Model Factors

We have found several amplification characteristics of the ground motion in the Taipei basin based upon the finite-difference calculation with a fine grid, high-resolution basin model. However, these amplification effects are controlled by several model factors. The variation of basement depth does not seem to be the most important factor to control the amplification. In order to know which factors dominate the wave amplification, we considered three different models: (1) a layered half-space model, (2) a basement structure model, and (3) a Songshan formation with a basement structure model. The layered half-space model 1 gives a 200-m-thick sedimentary layer with P -wave velocity 3.0 km/sec over a 4.5 km/sec homogeneous half-space. Model 2 removes the Songshan formation and preserves only basin basement geometry. Model 3 contains all information including Songshan formation and basin basement structure, which is the model used in our previous study. Figure 9 shows the comparison of snapshots between the three testing models. The layered half-space model 1 has clear P wave, S -wave, and some later reflection phases with constant propagation times and concentric wavefronts (Fig. 9a). This model does not give rise to any reflected energy from the basin boundary (as there is none) when the wavefront passes through the study region. Model 2 produces some surface waves as the S wave propagates into the basin (Fig. 9b). However, this model gives rise to weak surface waves and a small number of reflected phases from the basin boundary. This phenomenon is a result of the gentle dipping of the basin boundary. At most of the basin boundary, the dip angle is less than 30° . Even for the steepest part at western basin edge, the dip angle is not more than 50° . This result indicates that the amplification effect is not solely the result of the basement geometry. Finally, the snapshot of model 3 shows an apparent surface wave within the basin (Fig. 9c). Total shaking time in the whole basin is about 60 sec, which is about two times the result from other models. With the Songshan formation,

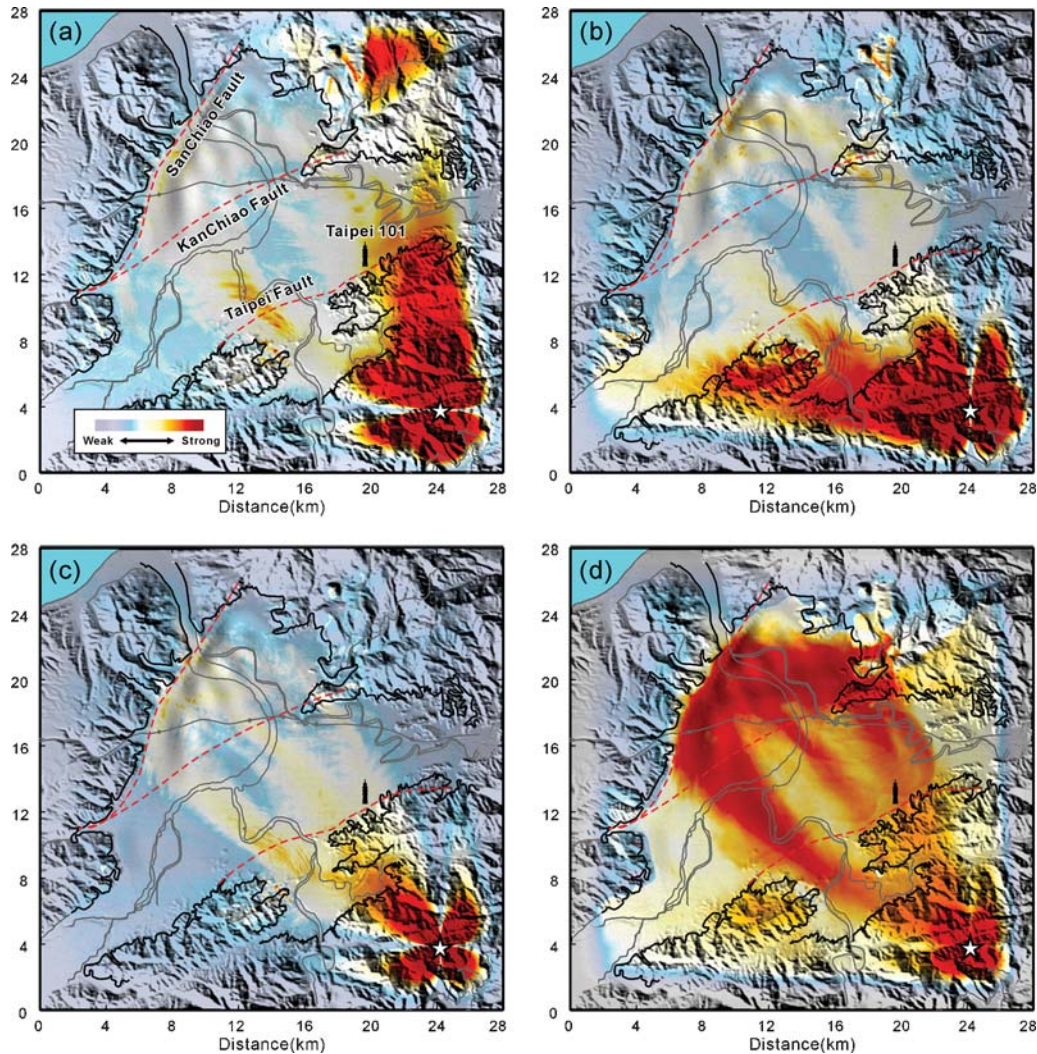


Figure 6. The PGV distribution derived from the point source simulation results in the (a) east component, (b) north component, and (c) vertical component. The cumulative kinetic energy distribution is presented in (d). The color bar in (a) shows the strength of the normalized value. The comparison points out that in the near-field region, cumulative kinetic energy E_k can provide a more accurate indicator of basin effect than PGV.

the model produces complex wave propagation behavior and shows the complexities of the basin effect, which are known in the previous analysis, including the amplification of surface waves and trapping of energy.

To examine the detailed difference between the three testing models, we analyze the E_k value along the pseudoarray as shown in Figure 10. For the layered half-space model (model 1), the E_k value does not have variation along the profile. It changes smoothly with azimuth, which responds to the influence of the source energy radiation pattern. The only basement structure model (model 2) has a large E_k value near the western boundary. This result shows the influence of pure basement geometry. The amplified E_k arises at the eastern and western basin, especially at the thinner part of the basement. However, the deepest part shows a relatively small E_k as compared to that at shallower part. It points out the basin depth can be one of the leading ampli-

fication factors as we consider only the basement geometry. In general, this model shows the overall trend of the E_k distribution, but the unusually large E_k at a specific place is not presented. Finally, the Songshan formation with a basement structure model has a complex E_k distribution (Fig. 10, model 3). It shows that the unusually large E_k at a local area might be from the appearance of the Songshan formation as compared to the results from model 2. The abnormally large E_k values are mostly located at locations that are filled with the thicker Songshan formation. This phenomenon is different from the basin structure model 2 that shows the amplification does not occur at the deepest part of the basement but at the shallow-and-vanishing part near the boundary. Although the deepest depth of the Songshan formation is only 120 m, and the average depth is less than 50 m within the basin, the simulation results indicate that the wave amplification may be mainly controlled by the presence of this

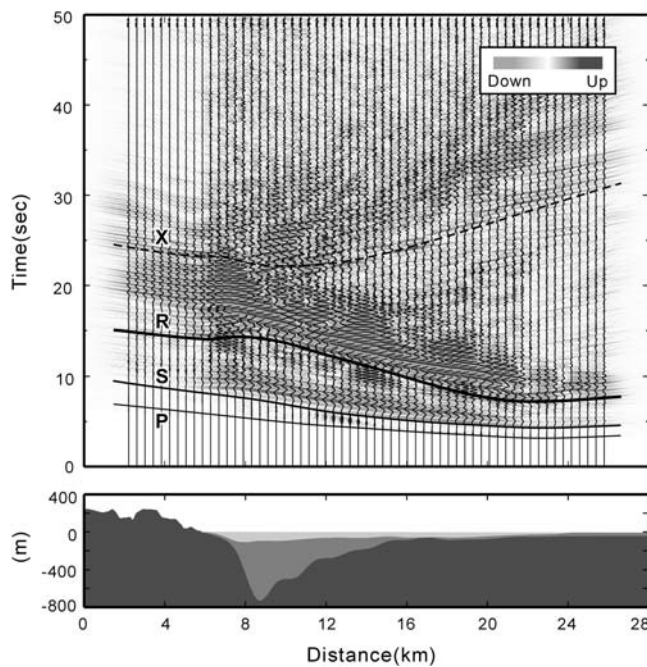


Figure 7. The 3D synthetic travel-time diagram along the west-east pseudoarray (light gray squares in Fig. 5). The gray scale indicates the strength and polarity of vertical component velocity records. Synthetic seismograms with a station interval of 400 m are also shown for comparison. Four main phases are marked as the (P) *P* wave, (S) *S* wave, (R) Rayleigh wave, and (X) radiation phase. Bottom panel shows the related cross section of the basin velocity model.

thin, near surface layer. The amplification result in this model is the largest among the three testing models. In this case, the average E_k ratio between inside and outside the basin is more than five times. From the E_k analysis, we conclude that the Songshan formation plays an important role that controls the dominant wave propagation behavior in the Taipei basin.

Frequency-Dependent Basin Amplification

Basin effects may depend on the frequency of the seismic waves. The frequency response of the Taipei basin model, containing Songshan formation and basin basement, is analyzed and shown in Figure 11. We compute the E_k values along the pseudoarray (Fig. 5) from seismic wave frequency between 0.25 and 4.0 Hz. The E_k amplification is defined as subtracting the E_k response of the half-space model from the basin model then dividing by the half-space response under the same frequency. We represent the E_k amplification value by percentage. In general, the lower the frequency the larger the amplification that occurs within the basin. High frequencies, such as 3 and 4 Hz, have average amplification values between 1 and 2. However, for the frequencies lower than 1 Hz, the average amplification value is about 3. The largest amplification is more than six, which occurred at the western basin boundary derived from 0.25 Hz. Although the amplification value is varied from dif-

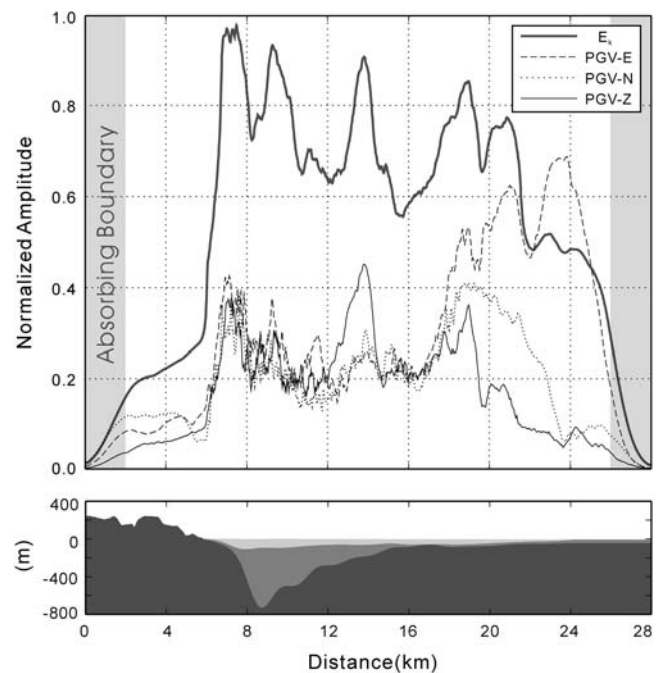


Figure 8. PGV and cumulative kinetic energy distribution along the pseudoarray. Three PGV components including east, north, and vertical are indicated by different types of thin black lines. The thick gray line is the E_k distribution. The area influenced by the absorbing boundary is marked by the shaded zone. Also shown in the lower panel is the velocity model across the profile.

ferent seismic wave frequencies, the overall distributions in the basin are similar, that is, the western area (deeper basin) is larger than the eastern area (shallow basin) and has a peak value at the western basin edge. Note that the amplification values derived from 1.0, 0.5, and 0.25 Hz are not changed too much. This result indicates that the major frequency response of the current Taipei basin model is closed to 1.0 Hz.

Simulations of the Real Data

The comparison between synthetic waveform and real data is important to validate the structural model and simulation result. However, the seismic activity within the Taipei metropolitan region has been few during past decades. Most of the reported earthquakes are small, which are hardly to be recorded comprehensively by the strong-motion network in the basin. In October 2004, a moderate earthquake (M_L 4.1) occurred near the southeast basin with depth 8.8 km, which was reported by CWB. Because the signal-to-noise ratios in most of the vertical component strong-motion records are poor, we choose the stations that have better record qualities in the horizontal component to compare with the simulation results. A Gaussian source time function with a duration of 0.8 sec is set up in the simulation. Both data and synthetic are band-pass filtered between 0.1 and 1.1 Hz and then normalized by the peak velocities of TAP089. Figure 12 shows the records and simulation results. For the stations close to the edge of the Taipei basin where the epicentral distances are

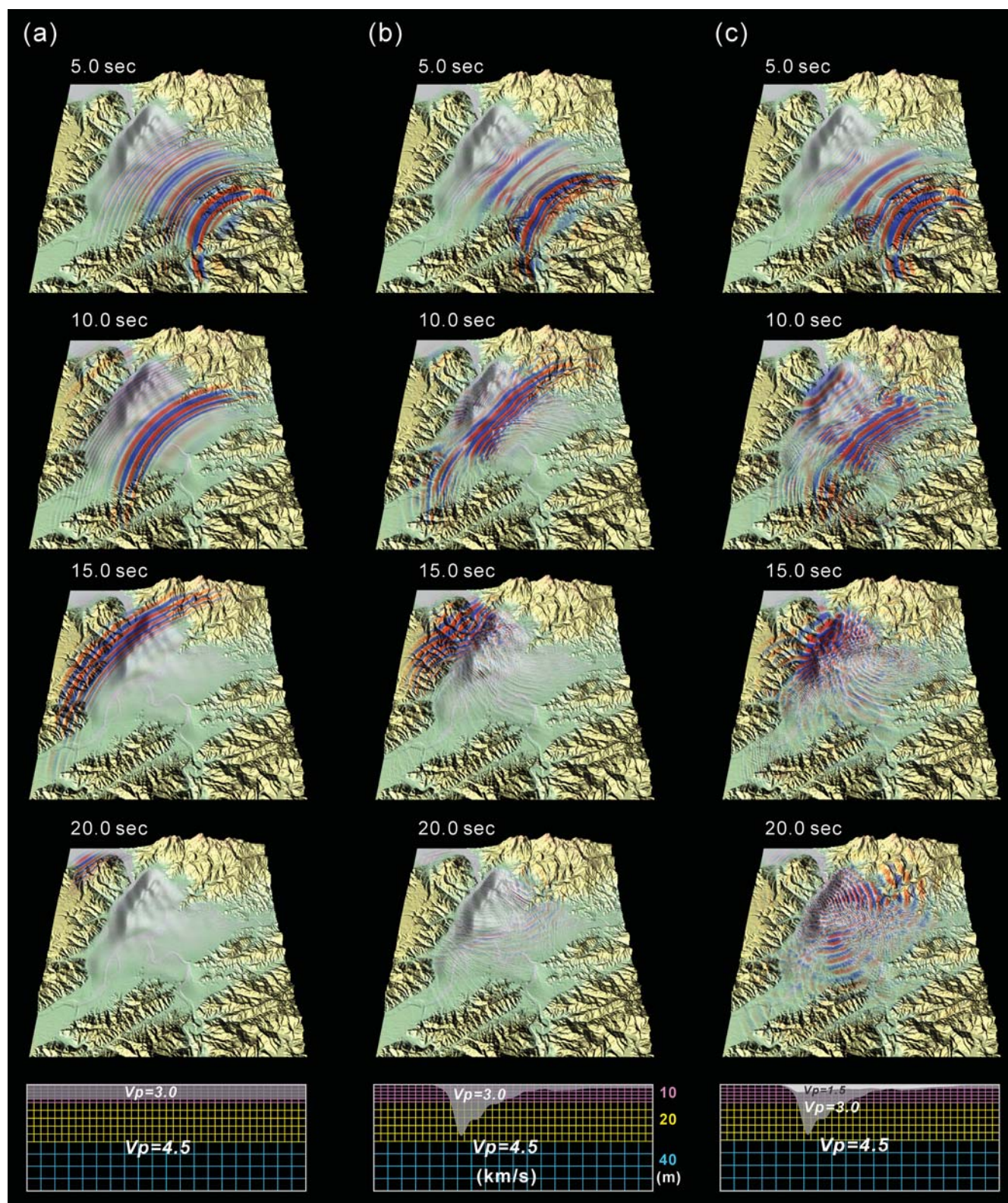


Figure 9. Snapshots derived from the three testing models: (a) the snapshots of layered half-space model; (b) the snapshots of the only basement structure model; and (c) the snapshots of the Songshan formation with a basement structure model. The bottom notes indicate the velocity profiles across the pseudoarray of these three testing models. Grid sizes in different computing domains are presented at the right side of model (b). It is clear that layered half-space model can not sustain energy after the wavefront passes through. A basement structure model displays a small amount of reflected energy from the basin boundary. Only the Songshan formation with the basement structure model can produce apparent basin effects.

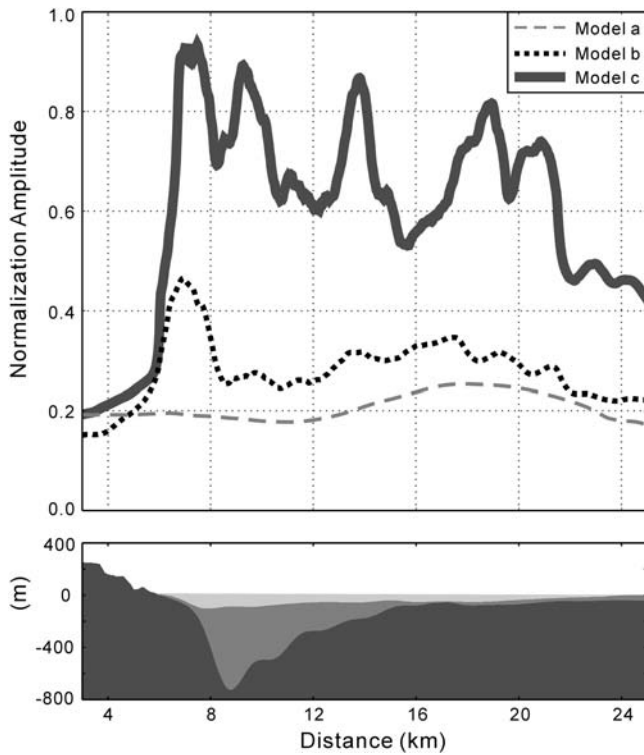


Figure 10. Distributions of the E_k value along the pseudoarray driven from the three testing models. Different types of gray lines are the E_k value derived from three models: (a) the layered half-space model; (b) only basement structure model; and (c) Songshan formation with a basement structure model. The lower sketch is the velocity structure across the profile in model (c). Results point out that the Songshan formation plays an important role that resulted in unusually large E_k at the local area for the wave propagated within the Taipei basin.

short, the data show smaller amplitude and simpler waveforms, such as TAP088 and TAP089. Our synthetics can match these observations well. For the stations at the eastern basin, for example, TAP015 and TAP092, the records show larger amplitudes (about 2–3 times compared to TAP089); still, the synthetic waveforms can explain the major phases sufficiently. Larger discrepancies occur when the stations approach the middle part of basin. These data have apparent amplified waveforms and complex later phases. Unfortunately, we do not have good records at the western basin to examine the simulation result where the ground shaking is expected to have the largest amplification and longer duration time.

In order to find out how to fill the gap between synthetic and observation at the middle part of basin, a sensitivity analysis on different S -wave velocities within the Songshan formation is considered. The simulation waveforms of station TAP021 are shown in Figure 13. Results indicate that the travel time of the major phases does not have significant influence. However, their amplitudes decrease and the later phases are stronger on the condition of slow S -wave velocity. A test on the heterogeneous velocity model (Wang *et al.*,

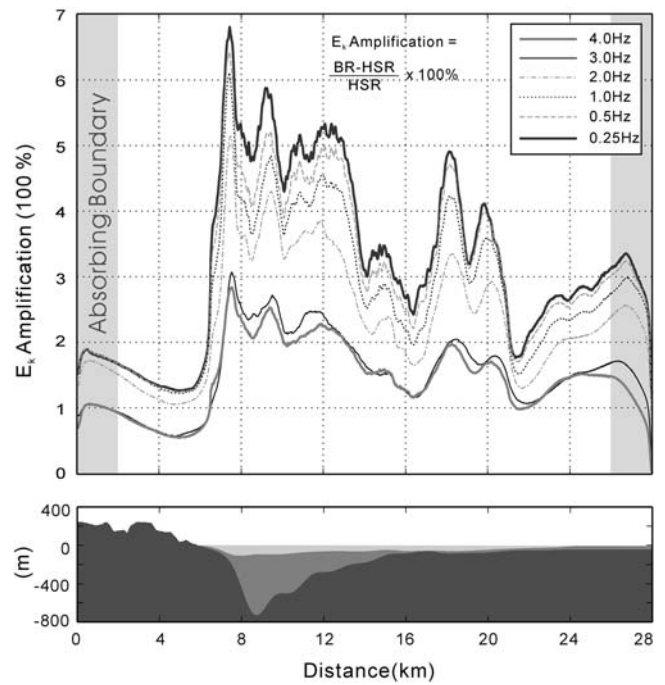


Figure 11. The basin amplification versus seismic wave frequency. We compute E_k along the pseudoarray from the frequency of 4.0, 3.0, 2.0, 1.0, 0.5, and 0.25 Hz. The E_k amplification is defined as subtracting the E_k response of half-space (HSR) from the basin model (BR), then dividing by the half-space response (HSR) under the same frequency. We represent the E_k amplification value by percentage. The amplification values from each frequency are indicated by different types of lines as described in the upper right legend.

2004) with lateral S -wave velocity variation at the shallow part of the basin (Table 1) is also considered. Because of the limitation of our computing capacity, we restricted the slowest S -wave velocity to 0.26 km/sec. The simulation result of the 23 October 2004 Taipei earthquake is shown in Figure 13. The synthetic waveform derived from the heterogeneous velocity model amplifies to about 30% of that in the original model, but the phases are shifted and changed, which is not comparable with the observation in Figure 12.

Although the records of this earthquake give limited information, the result of waveform comparison indicates that the current Taipei basin model may not be sufficient to present the details of basin complexity. Furthermore, the source parameters of this earthquake (including magnitude, location, and focal mechanism) might also need a further validation for the purpose of near-field strong-motion simulation (Lee *et al.*, 2006). In the present study, we put emphasis on the amplification effects derived from the basin sediments and basin geometry. Although there are discrepancies between the models and the realistic structure, the general Taipei basin amplification effects have been outlined. Our future study will take other factors into account, such as surface topography and finite dimensions of the source model to shed light on a realistic scenario of seismic hazard analysis.

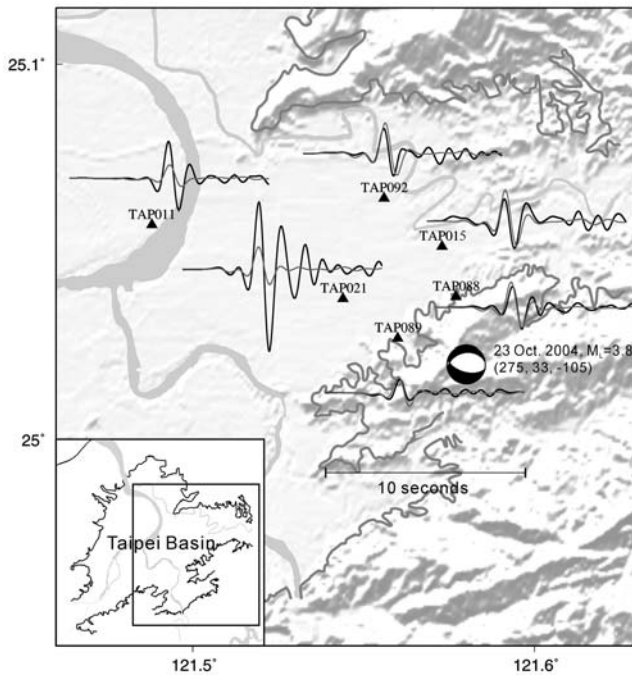


Figure 12. Comparison between observed and synthetic waveforms. The strong-motion records of the 23 October 2004, Taipei earthquake (M_L 3.8) are used to examine the simulation results. Black lines are the observations; gray lines show the synthetic waveforms derived from the finite-difference simulation. All the waveforms are velocity type in the north component. Both data and synthetics are normalized by the reference station, TAP089. The hypocenter (121.57° E, 25.02° N, depth 9.2 km) and focal mechanism (strike, 275° ; dip, 33° ; rake, -105°) are indicated by the black-and-white symbol, which is reported from the CWB.

Conclusions

This study provides a general seismic strong shaking analysis examining a basin with complex shallow geometry and filled with very soft sediments. We used a discontinuous grid finite-difference method to analyze the wave propagation behavior within the Taipei basin. By taking advantage of a discontinuous grid, a grid space with 20 m in the shallowest part is considered. Both the basin geometry and low velocity surface sediments (the Songshan formation) can be taken into account with high accuracy. A double-couple point source is assumed, located at the southeast part of the analysis and with a depth of 1 km, to simulate the possible damaging motions of a shallow regional earthquake. Our results indicate that the near-field PGV distribution is easily influenced by the source radiation. However, the cumulative kinetic energy E_k shows a clear basin effect. The amplification characteristics include (1) surface waves generated by the primary S wave trapped at the shallow part of the basin; (2) at the northwestern edge of the basin, most of the seismic waves rebounded from the basin boundary and focused upon the deepest part of the basin, generating large-amplitude waves due to basin reverberations and prolonged shaking in the basin; and (3) increased energy becomes apparent with

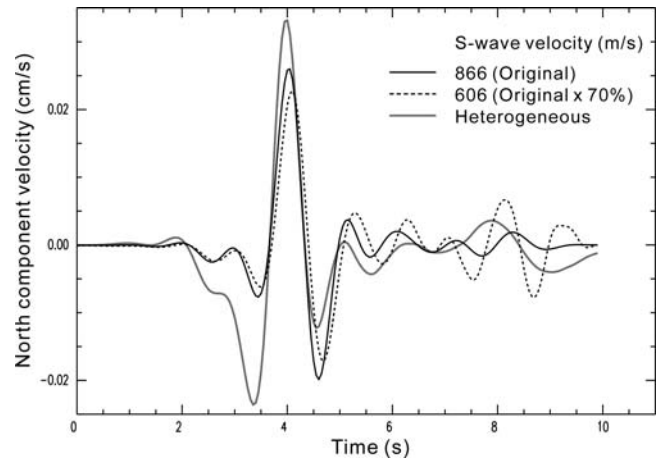


Figure 13. Sensitivity analysis on different S -wave velocities within the Songshan formation and heterogeneous velocity model (Table 1). The velocity type, north component, synthetic waveforms at station TAP021 are shown. Solid line is the result of original model with constant S wave ($V_s = 866$ m/sec) for the Songshan formation; dotted line is the result derived from 70% of the S wave in the original model ($V_s = 606$ m/sec). The synthetic waveform resulted from heterogeneous velocity model that contains lateral S -wave velocity variation in the Songshan formation is shown by the gray line.

noticeable wave radiation toward the east and south. At the same time, the deepest part of the basin reverberates with a period of about 2 sec. Our results indicate that the geometry of the basement structure alone cannot effectively produce the surface wave and reflection phases. This result may be controlled by the variation of the dipping angle on the basin boundary. However, the depth variation of the Songshan formation with low S -wave velocity near the surface can amplify seismic waves. We conclude that the Songshan formation plays an important role when energy propagates in the Taipei basin. Therefore, for the purpose of strong ground motion prediction, using scenario earthquakes with high-resolution geographical and geologic information is necessary in any seismic hazard analysis in the future.

Acknowledgments

The authors would like to thank C. Y. Wang and the Earthquake and Shallow Reflection Seismic Lab at National Central University (NCU) for providing the Taipei basin digital model data used in this study. We thank K. F. Ma for the discussions and the support of the computing facility during the study. We would also like to thank Ta-Liang Teng for detailed and critical reviews. Special thanks go to the Institute of Earth Sciences, Academia Sinica (IESAS) and the Seismological Lab at California Institute of Technology (Caltech) where many valuable discussions occurred. We also thank Dr. Hiroshi Kawase and three anonymous reviewers for their constructive comments on improving the manuscript. This research was supported by Academia Sinica, Taiwan, Republic of China, under Grant Number AS-94-TP-A08.

References

- Alex, C. M., and K. B. Olsen (1998). Lens-effect in Santa Monica, *Geophys. Res. Lett.* **25**, 3441–3444.

- Aoi, S., and H. Fujiwara (1999). 3-D finite-difference method using discontinuous grids, *Bull. Seismol. Soc. Am.* **89**, 918–930.
- Cerjan, C., D. Kosloff, R. Kosloff, and M. Reshef (1985). A nonreflecting boundary condition for discrete acoustic and elastic wave equations, *Geophysics* **50**, 705–708.
- Chang, W. F., and G. A. McMechan (1987). Elastic reverse-time migration, *Geophysics* **52**, 1367–1375.
- Chang, W. F., and G. A. McMechan (1994). 3-D elastic prestack reverse-time depth migration, *Geophysics* **59**, 597–609.
- Chen, K. C. (2003). Strong ground motion and damage in the Taipei basin from the Moho reflected seismic waves during the March 31, 2002, Hualien, Taiwan earthquake, *Geophys. Res. Lett.* **30**, 1151–1154.
- Clayton, R. W., and B. Engquist (1977). Absorbing boundary conditions for acoustic and elastic wave equations, *Bull. Seismol. Soc. Am.* **6**, 1529–1540.
- Davis, P. M., J. L. Rubinstein, K. H. Liu, S. S. Gao, and L. Knopoff (2000). Northridge earthquake damage caused by geologic focusing of seismic waves, *Science* **289**, 1746–1750.
- Graves, R. W. (1998). Three-dimensional finite-difference modeling of the San Andreas fault: source parameterization and ground-motion levels, *Bull. Seismol. Soc. Am.* **88**, 881–897.
- Gropp, W., E. Lusk, N. Doss, and A. Skjellum (1996). A high-performance, portable implementation of the MPI message passing interface standard, *Parallel Comput.* **22**, 789–828.
- Komatitsch, D., Q. Liu, J. Tromp, P. Suss, C. Stidham, and J. H. Shaw (2004). Simulations of ground motion in the Los Angeles basin based upon the spectral-element method, *Bull. Seismol. Soc. Am.* **94**, 187–206.
- Lee, S. J., H. W. Chen, and K. F. Ma (2007). Strong ground motion simulation of the 1999 Chi-Chi, Taiwan, earthquake from a realistic 3D source and crustal structure, *J. Geophys. Res.* **112**, B06307, doi 10.1029/2006JB004615.
- Lee, S. J., B. S. Huang, and W. T. Liang (2006). Grid-based moment tensor inversion by using spectral-element method 3-D Greens functions (Abstract S11C-0137), *EOS Trans. AGU* **87**, no. 36 (West. Pac. Geophys. Meet. Suppl.), S11C-0137.
- Olsen, K. B. (2000). Site amplification in the Los Angeles basin from three-dimensional modeling of ground motion, *Bull. Seismol. Soc. Am.* **90**, S77–S94.
- Olsen, K. B., R. J. Archuleta, and J. R. Matarese (1995). Three-dimensional simulation of a magnitude 7.75 earthquake on the San Andreas fault, *Science* **270**, 1628–1632.
- Olsen, K. B., J. C. Pechmann, and G. T. Schuster (1996). An analysis of simulated and observed blast records in the Salt Lake basin, *Bull. Seismol. Soc. Am.* **86**, 1061–1076.
- Wang, C. Y., Y. H. Lee, M. L. Ger, and Y. L. Chen (2004). Investigating subsurface structures and P- and S-wave velocities in the Taipei basin, *TAO* **15**, 222–250.
- Wen, K. L., and H. Y. Peng (1998). Site effect analysis in the Taipei basin: results from TSMIP network data, *TAO* **9**, 691–704.
- Wen, K. L., L. Y. Fei, H. Y. Peng, and C. C. Liu (1995). Site effect analysis from the records of the Wuku downhole array, *TAO* **6**, 285–298.
- Yomogida, K., and J. T. Etgen (1993). 3-D wave propagation in the Los Angeles basin for the Whittier-Narrows earthquake, *Bull. Seismol. Soc. Am.* **83**, 1325–1344.

Institute of Earth Sciences
Academia Sinica
Nankang, Taipei 115, Taiwan, Republic of China
sjlee@earth.sinica.edu.tw
hwbs@earth.sinica.edu.tw
(S.-J.L., B.-S.H.)

Institute of Geophysics
National Central University
Jung-Li 320, Taiwan, Republic of China
hwchen@earth.ncu.edu.tw
(H.-W.C.)

Manuscript received 28 April 2006